Diffusion Tensor Magnetic Resonance Imaging-Derived Myocardial Fiber Disarray in Hypertensive Left Ventricular Hypertrophy: Visualization, Quantification and the Effect on Mechanical Function

Archontis Giannakidis, Damien Rohmer, Alexander I. Veress, Grant T. Gullberg

CHAPTER 53

Diffusion Tensor Magnetic Resonance Imaging-Derived Myocardial Fiber Disarray in Hypertensive Left Ventricular Hypertrophy: Visualization, Quantification and the Effect on Mechanical Function

Archontis Giannakidis[1], Damien Rohmer[2], Alexander I. Veress[3] & Grant T. Gullberg[1,4]

[1]Lawrence Berkeley National Laboratory, Berkeley, CA, USA
[2]INRIA, Lyon & Grenoble University, Lyon, France
[3]University of Washington, Seattle, WA, USA
[4]University of California San Francisco, San Francisco, CA, USA

Abstract

Left ventricular hypertrophy induced by systemic hypertension is generally regarded a morphological precursor of unfortunate cardiovascular events. Myocardial fiber disarray has been long recognized as a prevalent hallmark of this pathology. In this chapter, *ex vivo* diffusion tensor magnetic resonance imaging is employed to delineate the regional loss of myocardial organization that is present in the excised heart of a spontaneously hypertensive rat, as opposed to a control. Fiber tracking results are provided that illustrate in great detail the alterations in the integrity of cardiac muscle microstructure due to the disease. A quantitative analysis is also performed. Another contribution of this chapter is the model-based assessment of the role of the myofiber disarray in modulating the mechanical properties of the myocardium. The results of this study improve our understanding of the structural remodeling mechanisms that are associated with hypetensive left ventricular hypertrophy and their role.

Introduction

Myocardium microarchitecture

The myocardium is primarily (75%) composed of a helical network of muscle fibers that twist around the heart. The muscle fibers (also known as myocytes) are shaped like cylinders of radius 5–10 μm and length 80–100 μm. To preserve the cardiac tissue architecture during the heart's large deformations due to contractile motion, the adjacent fibers are embedded in an extracellular matrix (ECM) called endomysium, that consists mainly (62%) of type III (highly deformable) collagen. Another role of ECM is to connect the myocytes to the myocardium's supporting coronary vasculature. In addition to fibers, another microstructural component of myocardial tissue is the cardiac laminar sheets, which are formed by stacking 3–4 fibers. This laminar structure is oriented transversly to the heart wall and is bounded by cleavage planes. The voids between laminae are occupied by a collagen network called perimysium. The principal constituent (72%) of perimysium is type I collagen (high tensile strength). A virtual representation of the cardiomyocyte compartment and its surrounding collagen network is given in Figure 53.1. For more details regarding the microarchitecture of cardiac muscle, the interested reader is referred to [1] and references therein.

Diffusion tensor magnetic resonance imaging

Within the hierarchical structure of the cardiac muscle described above, water molecules are transported by random thermal collisions. However, this drifting, which occurs even in the complete absence of bulk flow, is not free. In particular, there is greater hindrance to water transport across a

Cardiac Mapping, Fourth Edition. Edited by Mohammad Shenasa, Gerhard Hindricks, Martin Borggrefe, Günter Breithardt, and Mark E. Josephson.

P1: SFK/UKS P2: SFK Color: 4C
BLBK431-c53 BLBK431-Shenasa July 25, 2012 10:23 Trim: 276mm X 219mm Printer Name: Yet to Come

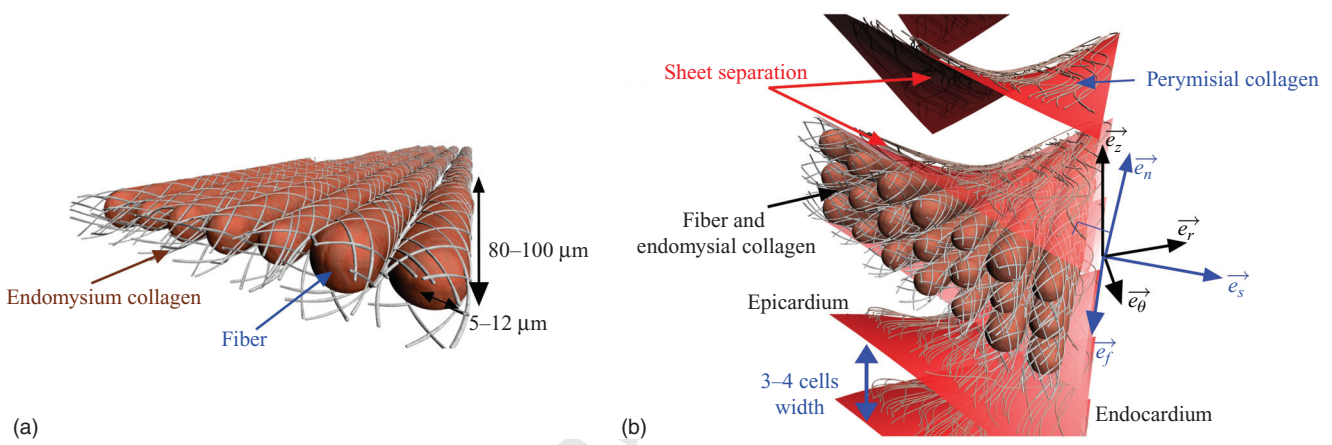

Figure 53.1 Schematic diagram of the two components of the cardiomyocyte compartment and the surrounding collagen network. (a) Cardiac myofibers, represented by the long oval structures, and the surrounding endomysium. (b) The laminar sheets of the heart. The layers consist of tightly coupled myocytes 3–4 cells thick, and are separated by cleavage planes. Also given are the orthonormal bases used to represent the heart wall and the laminar sheets in a Lagrangian coordinate system. (From Rohmer D, *et al. Invest Radiol* 2007;**42**:777–89, with permission.)

cardiac muscle fiber than along it. Consequently, the mobility of water becomes greatest along the long axis of the fibers. In a similar manner, the cleavage planes that physically separate the cardiac sheets act like a barrier to water diffusion. This causes the diffusion to be less in the normal direction of the laminar sheets than within the sheets. From the description above, it is obvious that by calculating the anisotropic water diffusion, one may infer information about (i) the microstructural organization of the myocardium, and (ii) the derangement of the normal microstructural patterns that is associated with certain cardiac diseases.

Diffusion tensor magnetic resonance imaging (DT-MRI) [2,3] has emerged as a powerful tool that performs this calculation. Unlike its predecessors (iontophoresis [4], photobleaching [5], etc.), DT-MRI (i) does not require some invasive labeling or monitoring procedure, (ii) does not require exogenous contrast agents, and (iii) is an inherently three-dimensional (3D) technique. DT-MRI characterizes the preferential water diffusion by a tensor field. The diffusion tensor is obtained voxel-by-voxel by fitting a set of N ($N \geq 6$) diffusion-weighted MRI acquisitions (each obtained with a different orientation and/or magnitude of the diffusion sensitizing gradient) and one diffusion-independent MRI reading. An excellent review of cardiac DT-MRI is presented in [6]. Apart from cardiac muscle, DT-MRI has also been employed to measure the anisotropy of water diffusion in other oriented tissues such as brain white matter [7], articular cartilage [8], spinal cord [9], tongue [10], breast [11], prostate gland [12], pelvic floor [13], thigh muscle [14] and calf muscle [15].

The *in vivo* DT-MRI imaging of myocardial microstructure is currently hindered by the long acquisition times that are necessary to tackle the inherently low signal-to-noise ratio (SNR) of this imaging modality [6]. Great sensitivity to beating heart and other motion artifacts, eddy current artifacts, partial volume effects and poor spatial resolution further degrade the *in vivo* DT-MRI cardiac images [6]. As a result, at present, the technique is mainly conducted *ex vivo* using excised fixed hearts.

Tracking of the microstructural components of myocardium

The diffusion tensor at each voxel contains information about the amount of water diffused as well as the orientations of the local fibers and laminar sheet surfaces. By exploiting the fiber-related directional information at all voxels, one may reconstruct and visualize the continuous 3D trajectories of fiber tracts throughout the myocardium by using a process called DT-MRI cardiac fiber tractography [16]. Likewise, by making use of the sheet inclination information that is incorporated in the discrete set of diffusion tensor data, the cardiac laminar sheet structure may be imaged. To add to the above applications, DT-MRI tracking of the myocardial microstructural components may be used to also render visible the structural remodeling in the presence of cardiac pathology.

Streamline tracking [1,17] is a common method used to reconstruct cardiac fibers and laminae. In this technique, the recovered trajectories and surfaces evolve incrementally. To minimize noise effects and achieve better smoothing, an anisotropic filtering method [18] may be employed before the tracking. Video clips 53.1 and 53.2 and Figure 53.2 show DT-MRI fiber and sheet tracking results that were obtained by applying the streamlining method [1] to the left ventricle (LV) of an excised adult male Wistar-Kyoto (WKY) rat heart.

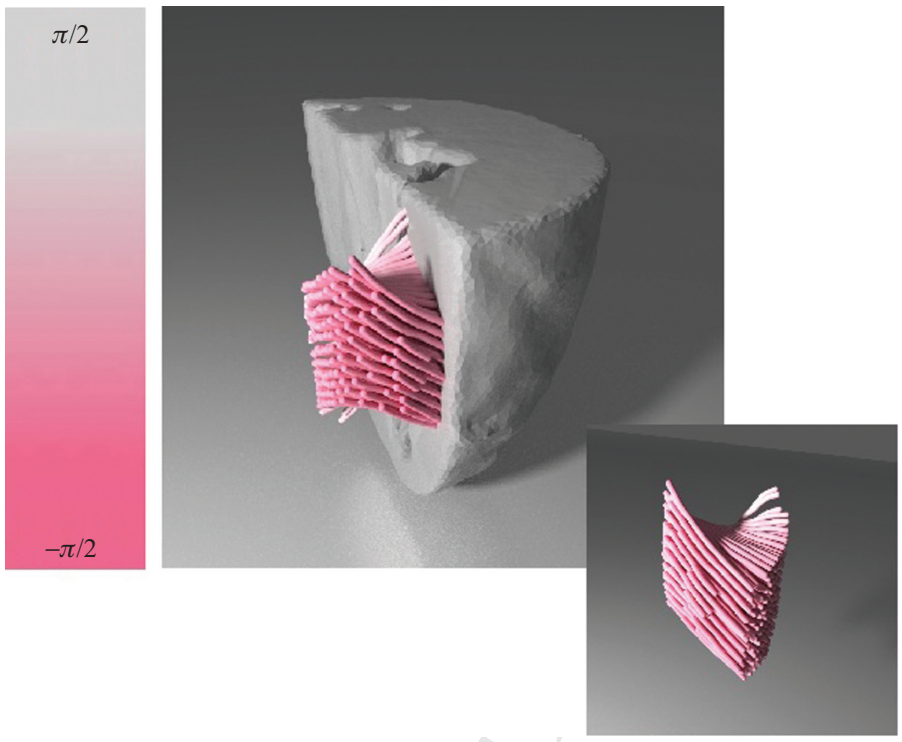

Figure 53.2 Fiber tracking results of a transmural block cut from the left ventricular wall of an excised adult male Wistar-Kyoto (WKY) rat heart. The classic counterclockwise epicardial-to-endocardial rotation of the cardiac muscle fibers may also be seen. The reconstruction results were obtained by using the streamlining method described in [1].

Hypertension-induced left ventricular hypertrophy as an ominous sign of heart failure

Left ventricular hypertrophy (LVH) [19,20] refers to the structural remodeling of the heart when it is exposed to sustained ventricular load. The increased afterload may be caused by physiological stimuli such as athletic exercise, or pathological stimuli such as hypertension, aortic stenosis or aortic insufficiency [20]. The pathologic case we study in this chapter is LVH induced by genetic systemic hypertension [21,22]. However, it is worth noting that not all hypertensive subjects develop LVH [23].

Hypertensive LVH is a complex and multi-factorial process. As well as the elevated blood pressure (hemodynamic component), factors such as demographics (age, sex, race, social class), concurrence of other pathological conditions (increased body mass index, insulin resistance syndrome) and genetics are among those that play a role in the development of LVH in hypertensive subjects [21].

The most prevalent morphological characteristic of LVH caused by arterial hypertension is the symmetric thickening of the LV muscle wall accompanied by an increase in the respective mass [19]. The increased ratio of wall thickness to cavity radius results in a concentric pattern of hypertrophy. Apart from this distinct change in cardiac wall geometry, an additional morphologic feature of the myocyte compartment is the disorientation of microstructural components [24]. At the same time, an intrinsic property of the cardiac muscle, the value of which has been shown to grow significantly as hypertensive LVH progresses, is myocardial stiffness [25]. In the non-myocyte connective network of the myocardium, structural changes associated with hypertension-induced LVH include the elevated collagen concentration (myocardial fibrosis or scar formation) [26]. Finally, extracellular alterations due to hypertensive LVH have also been observed in the microcirculation. These include decreased capillary density, peri-vascular fibrosis and medial thickening of intramyocardial coronary arteries [27,28].

There are molecular mechanisms that underlie the transduction of the increased LV wall tension (mechanical information) present in hypertensive subjects to the myocardial enlargement described. The biomechanical transduction that induces the structural remodeling is described briefly here [20,29–31]. At first, signaling molecules such as calpain proteases, growth factors, cytokines and neurohormones are recruited as mediators. These signaling molecules bind to specific receptors (such as kinases and integrins) that are found on the surface of cardiomyocytes. Next, the receptors activate intracellular signaling cascades (in this way they communicate their signals to the nucleus of myocytes) that promote (i) modifications in gene transcription and (ii) increased synthesis of the protein contractile units (sarcomeres). The parallel addition of sarcomeres produces an increase in the size of the myocytes, which, in turn, leads to cardiac wall thickening. Coordinated molecular changes occur also at the surrounding collagen network, where the increased activation (upregulation of genes) of the matrix metalloproteinases (MMPs) appears to play a major role in

P1: SFK/UKS P2: SFK Color: 4C
BLBK431-c53 BLBK431-Shenasa July 25, 2012 10:23 Trim: 276mm X 219mm Printer Name: Yet to Come

controlling the remodeling (i.e., increased collagen content) of ECM [29]. To sum up, the gross structural remodeling in LVH that occurs in hypertensive subjects is a change collectively brought about by molecular, cellular, and biochemical events. In addition, the development of LVH is mediated by neurohormones released by the sympathetic and renin–angiotensin–aldosterone systems [32–34]. This is of particular interest, since these neurohormonal systems are amenable to pharmacological manipulation [21,34].

Even though the early stage of the myocardial structural remodeling in the presence of hypertension is generally regarded as a useful compensatory mechanism that allows a normal LV stroke volume and minimizes stress, these structural alterations have also been held responsible for the impaired physiological function that comes along with this pathological remodeling, and are generally considered a morphological precursor of adverse cardiovascular outcomes [21,35]. In the following, we outline the physiological alterations that have been interpreted by the structural remodeling in hypertensive LVH, and also elaborate why these functional changes represent clinical manifestations of certain associated diseases.

Electrical remodeling is closely related to structural remodeling, whereby a substrate for triggering and maintenance of arrhythmias is created [36]. The presence of arrhythmias in hypertensive LVH is associated with increased incidence of sudden death [37,38]. Similarly, the structural changes have a direct bearing on the mechanical function of the heart where an impairment of the diastolic [39–43] and systolic [44,45] functions and the synchronicity [46] of these two has been observed in subjects with hypertensive LVH. This abnormal mechanical function of the LV has been documented [29] to be a major cause of congestive heart failure (CHF). That being said, epidemiological studies have indicated [47] that in 75% of patients who developed CHF arterial hypertension with definite signs of LVH had been diagnosed. We have already mentioned that a common structural alteration in subjects with hypertensive LVH is the medial thickening of the intramyocardial coronary arteries. This characteristic predisposes such patients to the development of coronary artery disease (CAD) or atherosclerosis [30,48]. However, CAD brings about obstruction in blood flow [41] which is another example of forthcoming complications. This physiological alteration, when coupled with the decreased capillary density, lead to decreased myocardial oxygen supply that facilitates the formation of microischemic regions [49,50]. Also, it has been shown [21,49] that apart from the abnormalities in coronary blood flow (vascular component), the increased wall thickness (myocardial component) further aggravates the development of ischemia in hypertensive subjects. Meanwhile, the reduced oxygen supply in the remodeled myocardium fails sooner rather than later to meet the increased myocardial demand of oxygen that the hypertensive LVH imposes (oxygen demand is proportional to the wall stress) [48,51]. This imbalance has been reported [52] to incite angina pectoris (chest pain), which, in turn, heralds myocardial infarction (MI) [50]. Both ischemia and MI cause a decline in cardiac pumping ability, and heart failure ensues naturally.

Currently, hypertensive LVH contributes significantly to the growing healthcare costs of cardiovascular diseases. An earlier diagnosis (before the overt transition to CHF), followed by treatment that aims at reversing this pathology, would help to improve wellbeing and stem increasing healthcare costs.

The role of mechanical modeling in cardiology

Finite element (FE) computational models of the heart provide an ideal hosting environment to observe the mechanical function of the heart, mainly due to their versatility. Apart from simulations of the normal cardiac function, they can also be used to study the alterations caused by cardiac disease. More importantly, by studying the progression of one disease, mechanical models may provide a way to better understand mechanical aspects that play a role in the development of that specific disease. Another advantage of computational modeling is the capability to evaluate some mechanical properties of the heart, such as the cardiac wall stress field, that cannot be experimentally measured by the currently available methods. This information could then be used, for example, to estimate material parameters by matching FE deformation or strain predictions with the measured values. A comprehensive overview of computational modeling from the solid mechanics perspective may be found in [53].

Contribution of this chapter

Myocardial disarray has been long recognized [24,54–58] as a prevalent pathological hallmark of LVH induced by arterial hypertension. It refers to the irregular arrangement in every level of myocardial organization, from the myofibrils and myofilaments to the fibers and fascicles. In this chapter we focus on the fiber level. The well-ordered and smoothly varying spatial alignment of myocardial fibers that characterizes the normal myocardium no longer exists in the areas of myofiber disarray.

However, until now, there have been no DT-MRI studies on delineating the spatial misalignment of myocardial fibers that is associated with hypertensive LVH. Instead, all previous related attempts [24,54–58] were made using light microscopy, a technique that is much more laborious, invasive, and time-consuming than DT-MRI. To our knowledge, this chapter is the first report of DT-MRI being employed to assess the geometric rearrangement of the cardiomyocytes, following hypertensive LVH.

By performing *ex vivo* studies in two excised hearts taken from a rat with hypertensive LVH and its normotensive equivalent, we first provide fiber tracking images that

pinpoint and illustrate in great detail the regionally disordered fiber orientation that is present in the pathologic case, as opposed to the normal case. Having identified the loss of the microstructural organization that is associated with hypertensive LVH, we take a further step by quantifying this myofiber disarray. The maps of fiber regularity in the myocardium are produced by relying on a novel scatter matrix-based approach. Another contribution of this chapter is the model-based assessment of the role of the myofiber disarray in modulating the mechanical properties of the myocardium with hypertensive LVH and the ascertainment of their relation.

Materials and methods

Research animal model

The spontaneously hypertensive rat (SHR) [59] is a well-established model of genetic hypertension. The development of this homozygous hypertensive rat strain was achieved by repeated selective breeding of WKY rats displaying the desired phenotype (high blood pressure) over several generations. Once the trait was fixed, sib mating was maintained for about 20 generations to achieve genetic homogeneity. In this particular strain of rat sustained, systemic hypertension invariably occurs accompanied by marked LVH [24]. Because the SHR provides a wide variety of genes to be inherited together, it is regarded [24] a reliable experimental model for studying essential hypertension in humans.

In this work, we performed *ex vivo* studies of one SHR fixed heart and one normotensive WKY fixed rat heart. The rats were bought from the Charles River Laboratories International, Inc., Wilmington, MA, USA. The age of both rats at the time of the heart excision was 22 months. The time period between excision and imaging was 25 days. All animal procedures conformed to the guidelines set forth by the Animal Welfare and Research Committee of Lawrence Berkeley National Laboratory.

Heart preparation

We induced anesthesia in the two rats by using isoflurane inhalation. When physical sensation was lost, the thorax was opened. Next, the intact heart was rapidly removed from the chest and flushed with warmed isotonic saline. Both hearts were arrested in end diastole. Once the hearts were rinsed, they were weighed and placed in 60 ml of 10% buffered formalin for fixation (i.e., prevention of tissue decay and maintenance of the diastolic shape). The myocardial mass normalized to the entire body weight was 0.38% for the WKY and 0.86% for the SHR rate. These parameter values served as confirmation of the presence of LVH in the SHR rat, as opposed to the WKY rat3.

Table 53.1 Imaging parameters used for each heart.

Scan of Fourier space	A 3D spin echo sequence was used
Field of view	$27 \times 15{:}5 \times 15{:}5$ (mm)
Voxel size	0.160 mm (isotropic)
Repetition time (T_R)	500 ms
Echo time (T_E)	19.224 ms
Number of averages	1
Slice thickness	0.160 mm (0 mm gap)
Number of slices	169
Matrix size	97×97
Gradient duration (δ)	4 ms
Gradient separation (Δ)	10 ms
Maximum strength of the gradient pulse (G)	30 G/cm
Diffusion-weighting factor (b)	1000 s/mm^2
Overall scan time	16 h 59 m 18 s 500 ms

Diffusion imaging

Scans of the whole hearts were carried out at the Small Animal MRI Imaging Facility of the University of Utah, using a Bruker BioSpec 7T horizontal bore MRI scanner. The optimized scheme of 12 gradient directions, proposed in [60], was used. One non-weighted image and 12 diffusion-weighted data sets were acquired for each heart. For the imaging, the specimens were placed in a susceptibility-matching solution called Fomblin which does not give a nuclear magnetic resonance (NMR) signal to increase contrast and eliminate susceptibility artifacts near the boundary of the heart. The long axis of each heart was aligned with the x-axis of the scanner. The imaging parameters are listed in Table 53.1.

Tensor data set reconstruction

The cardiac diffusion tensor field estimation was an overdetermined problem, since the measurements outnumbered the unknowns (i.e., we had 13 measurements for 6 unknowns). The solution was obtained by applying a nonlinear least-squares fitting algorithm [61].

Visualization of the myocardial fiber disarray using DT-MRI fiber tractography

First, recall that the DT-MRI measurement output is given as a volumetric discrete data set where each voxel contains the diffusion information along three global axes. For each voxel, the diffusion tensor can be expressed as a symmetric positive-definite matrix, and therefore decomposed into eigen-components, such that the eigenvectors give the main directions of diffusion while the eigenvalues are related to the magnitude of diffusion along the directions of the related eigenvectors. As the diffusion acts mainly along the fiber

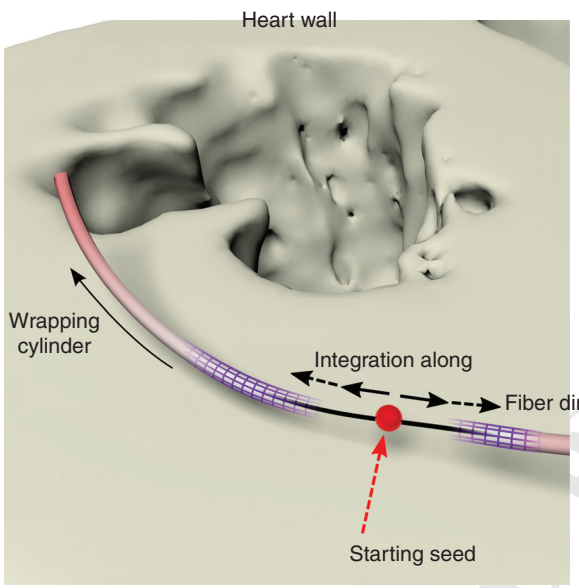

Figure 53.3 Illustration of the fiber tracking algorithm. Starting from an initial seed position, integration is carried out in both directions.

direction, it has been demonstrated [62] and validated [62] that the eigenvector associated with the greatest eigenvalue coincides with the local fiber orientation. Moreover, the smallest eigen-component may be considered as normal to the sheet structure, as it is related to the direction where the diffusion is minimal [1]. Therefore, sorting the three eigen-components with respect to their eigenvalues enables one to access the direction of the local fibers and sheets. In this section, we deal only with the tracking of cardiac muscle fiber tracts.

The algorithm we used is shown in Figure 53.3. First, an intensity-based automatic segmentation of the heart wall was performed based on the standard MRI acquisition. Next, 3D positions were evenly distributed within the heart wall to act as starting seeds of the fiber trajectory. For each seed position, the trajectory was computed as a streamline integration along the primary eigenvector. The integration was performed in both forward and backward directions of the fibers and continued as long as the trajectory stayed within the heart wall.

In practise, we used a step size of 90 μm on a grid of 169 × 97 × 97 voxels, where each voxel was a cube of 160 μm edge length. When about 3000 fiber trajectories were computed as polylines, we generated a sweep surface using cylinders of constant radius of 32 μm, wrapping each fiber trajectory to improve depth perception. The resulting cylinders are color encoded by the local fiber helix (inclination) angle, defined (according to the convention described in [63]) as the angle between the local circumferential direction and the projection of the fiber direction on the plane perpendicular to the local transmural direction (see Figure 53.1). The final rendering was performed using an offline ray-tracing algorithm. For the implementation of the algorithm, the open source software Sunflow (http://sunflow.sourceforge.net/) was employed. For more details regarding the fiber tracking method, see [1].

We performed qualitative comparison between the fiber tractography results obtained from the SHR and those obtained from the WKY. The presence of extensive fiber disarray in the lateral wall of the SHR, as opposed to the WKY, was revealed (see Figures 53.4 and 53.5 and Video clip 53.3).

Having recognized the spatial malalignment of myocardial fibers that is associated with hypertensive LVH, we now go on to quantify this myofiber disarray.

DT-MRI quantitative study of the myocardial fiber disarray

Regions of interest

We analyzed the inferolateral wall of the largest equatorial (mid-ventricle) short-axis slice (Figure 53.6) of the two rat

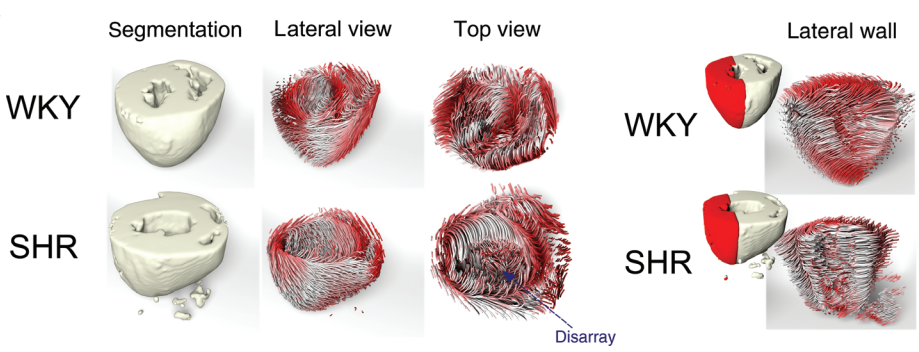

Figure 53.4 Fiber tractography results from the normal WKY (top) and the diseased SHR (bottom) rats. First column: The MRI-based segmented myocardia, where the hypertrophied cardiac wall of the SHR may be seen. Second and third columns: Two different views of the fiber tracking results of the entire wall. Seen from the top, there is marked myofiber disarray in the lateral region of the SHR, as opposed to the WKY. Last column: A close-up, focusing on the free wall region where the disarray in the SHR is more noticeable (see also Video clip 53.3).

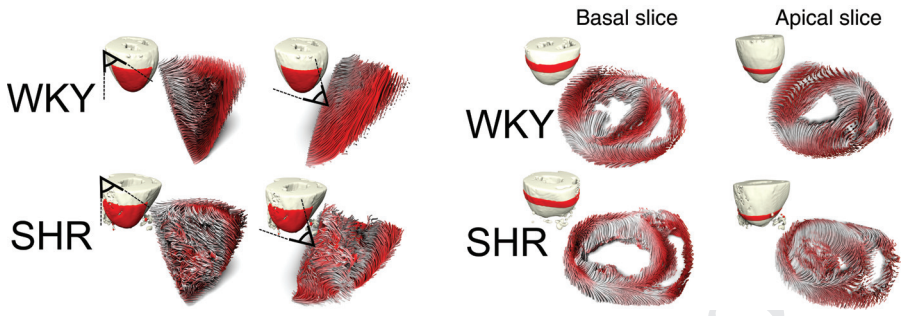

Figure 53.5 Left two columns: Two viewings (taken from two different angles) of the endolateral region of the normal (WKY) and the diseased (SHR) rats that demonstrate the presence of extensive disarray in the SHR, as opposed to the WKY. Right two columns: Fiber tracking results in slices located in the basal and apical region. Note that the disarray in the SHR is more prominent in the apical slice (see also Video clip 53.3).

hearts. The papillary muscles of the hearts were excluded from our analysis. In addition, diffusion tensors which had negative eigenvalues were considered to be noise and those voxels were excluded from our analysis. To obtain the binary masks of the regions of interest (ROIs), we partitioned the myocardium by using a spline-based segmentation. Zoom-ins of the qualitative fiber tracking results on the chosen ROI are shown in Figure 53.7 for the two rat hearts.

Quantitative analysis of myocardial fiber disarray

To spatially map the disarray of the myocardial fibers, we relied on the intervoxel diffusion coherence (IVDC) index [64]. The IVDC is an anisotropy measure of the scatter matrix [65] with respect to the primary diffusion eigenvectors. This index has also been used in the past [64] to characterize brain tissue organization. To the best of our knowledge, this is the first time that the IVDC has been used to quantify the derangement of cardiac myofibers.

When compared with other diffusion anisotropy indices, such as the fractional anisotropy (FA) or the relative anisotropy (RA), IVDC provides more explicit information about fiber regularity. In addition, IVDC is not restricted to studying intravoxel effects caused by biophysical tissue properties. Instead, for a given arbitrary voxel that lies on the cardiac wall, IVDC contains [65] information about the angular uniformity of the cardiac fibers within the neighborhood that consists of the voxel itself and its 26 nearest neighbors (spanning the same short-axis slice and the slices directly above and below). Moreover, unlike the visually appealing red–green–blue (RGB) color maps and cardiac fiber tractography methods, the IVDC lends itself to quantitative analysis of the cardiac fiber organization. In addition, it has the further favorable property of being insensitive to the sign of the eigenvectors.

The IVDC takes values from 0 to 1. Taking into account that the concept of "orientation coherence" is inversely proportional to the concept of "disarray," a large value of IVDC at a given voxel indicates that the disarray is insignificant in this voxel's neighborhood, whereas smaller values of IVDC denote a great loss of myocardial fiber organization. By calculating the IVDC at each voxel, maps of the whole myocardium may be obtained. The quantitative maps of

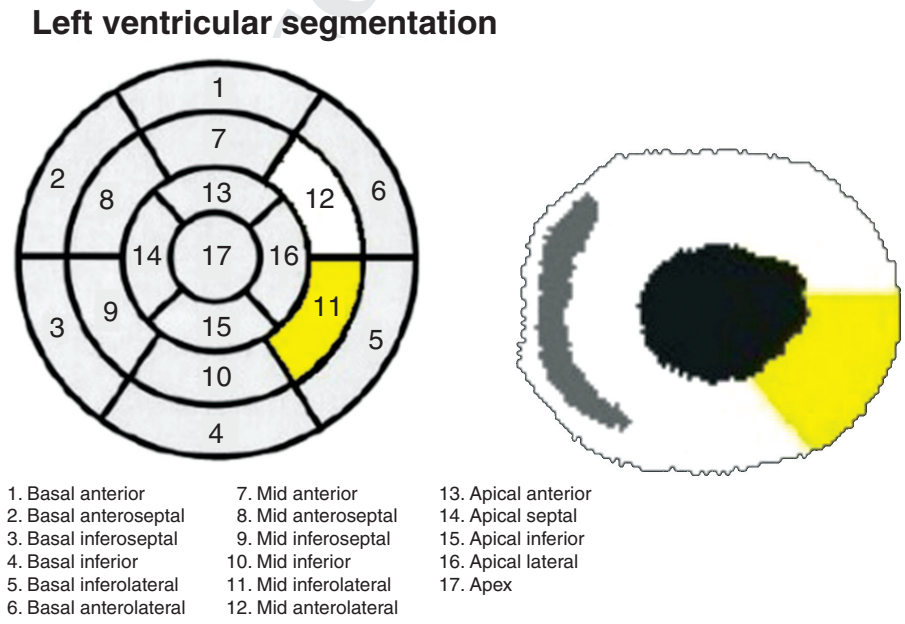

Figure 53.6 The region of interest (ROI) for this quantitative study.

P1: SFK/UKS P2: SFK Color: 4C
BLBK431-c53 BLBK431-Shenasa July 25, 2012 10:23 Trim: 276mm X 219mm Printer Name: Yet to Come

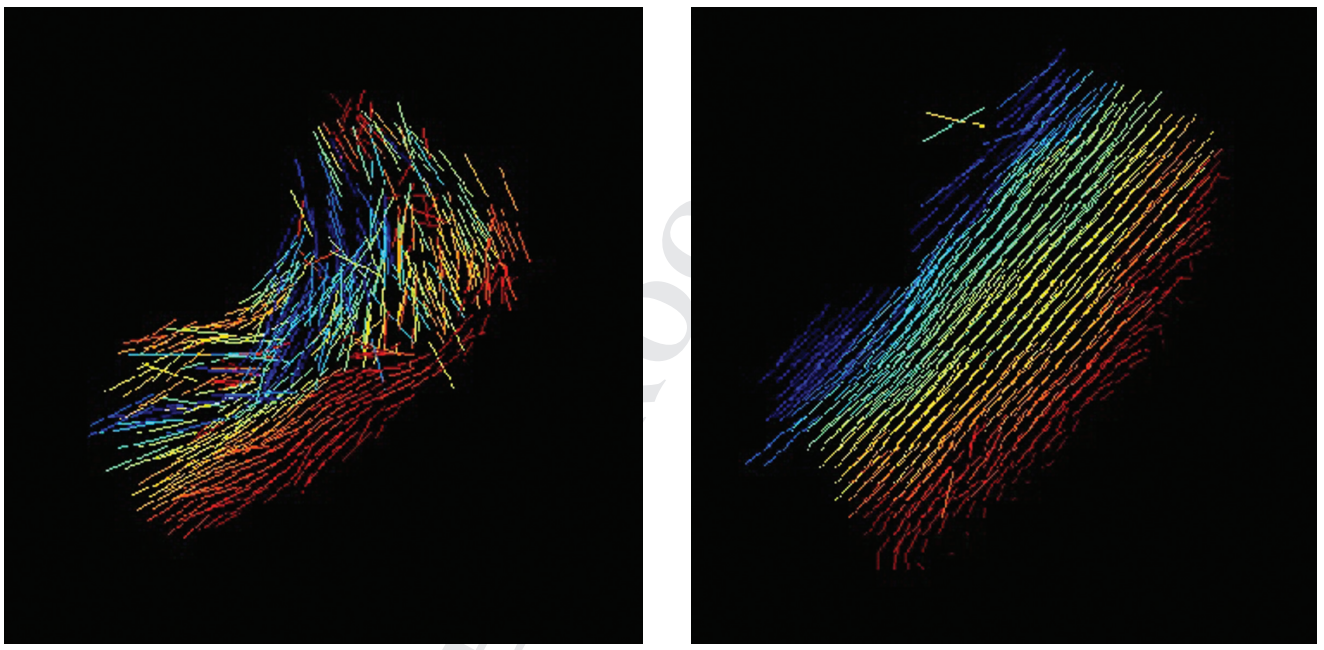

Figure 53.7 Zoom-ins of the qualitative fiber tracking results on the region of interest: SHR (a) and WKY (b). The results are color encoded by the local fiber helix (inclination) angle.

myofiber orientation coherence for the ROI are shown in Figure 53.8. It is easy to see that there is a highly coherent cardiomyocyte organization throughout the ROI of the WKY (witnessed by the white color in the whole respective map), while at the same time in the ROI of the SHR there are extensive areas with non-collinear myofiber distribution (denoted by the darker regions in the respective map). Values derived from statistical analysis of the quantitative results are summarized in Table 53.2. The interpretation of these statistics is that the difference in the DT-MRI-derived average fiber regularity between SHR and WKY is considered to be of extremely significant ($P < 0.0001$).

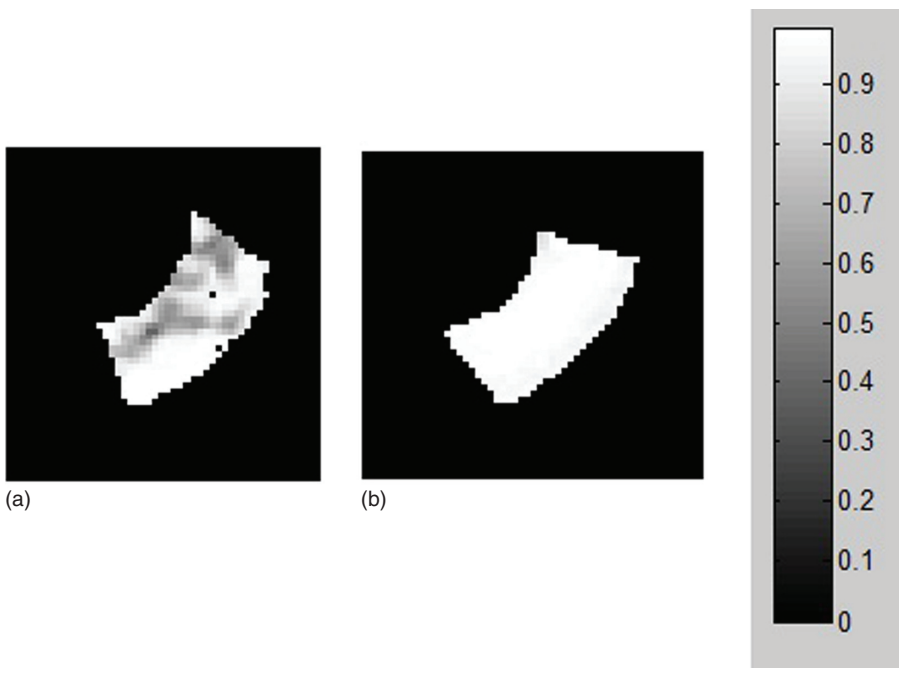

Figure 53.8 Quantitative myofiber orientation coherence maps in the region of interest: SHR (a) and WKY (b). The lighter the color at a voxel, the better fiber regularity (microstructural organization) in the neighborhood of the specific voxel. The darker areas denote the presence of extensive myofiber disarray.

P1: SFK/UKS P2: SFK Color: 4C
BLBK431-c53 BLBK431-Shenasa July 25, 2012 10:23 Trim: 276mm X 219mm Printer Name: Yet to Come

Table 53.2 Statistical analysis of the quantitative results.

	Mean	Standard deviation
WKY	0.9742	0.0189
SHR	0.8432	0.1431

The myocardial fiber disarray, a hallmark of LVH induced by systemic hypertension, was thus identified and quantified in our animals. In the next section, we provide evidence regarding the cause-and-effect relationship between the myofiber disarray in hypertensive LVH and the mechanical function of the LV.

Mechanical effects of myocardial fiber disarray: a model-based study

As already mentioned, one of the primary manifestations of LVH due to systemic arterial hypertension is impaired mechanical function. This decline in the LV ventricular wall performance was also witnessed in the diseased animal (SHR) of this study where the significant decrease in first principal strain seen in Figure 53.9 is also attributed to the progression of hypertrophy (as well as to aging).

The critical factors that account for mechanical dysfunction in the hypertensive LVH are primarily related to the structural remodeling. They include fibrotic stiffening [25, 30], myocardial scarring [21,30], myocardial fiber disarray [24], cardiomyocyte hypertrophy [30,41] and configuration of collagen with respect to the muscle cells [26,41]. The topic of investigation in this section is how myocardial fiber disarray contributes to abnormalities in mechanical function.

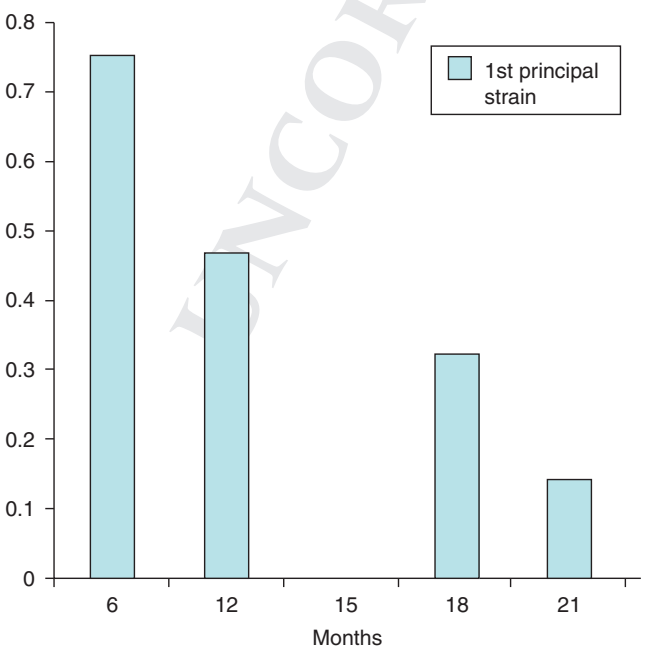

Figure 53.9 Plot of first principal strain for the SHR studied in the previous two sections.

The mechanical effects associated with the fiber disarray alone may be illustrated by making use of an existing FE model of the left ventricular wall [66,67]. This LV model has been shown [66,67] to be able to reproduce the gross geometric changes of the normal heart as well as the strain distributions found in the literature for normal function. To our knowledge, no other model of hypertrophied LV due to systemic hypertension has been developed in the literature. To incorporate the fiber disarray in the FE model, we altered [68] the normal fiber orientation distribution through the addition of randomly generated offsets to the two angles used to specify the myofiber orientation: (i) the inclination angle defined earlier, and (ii) the transverse angle, defined as the angle between the local circumferential direction and the projection of the fiber direction on the plane perpendicular to the local longitudinal direction (see Figure 53.1).

The amount of randomness of the fiber orientation distribution was controlled by specifying the range over which random numbers were generated. For example, specifying a randomness of values in the range of 4 would produce randomly generated numbers −2, −1, 0, 1 and 2. These randomly generated numbers were then added to the original fiber inclination and transverse angles specified for the normal model. Given an inclination or transverse angle of 45° and a randomness range of 4, the fibers may have orientations from 43° to 47°. FE models having the following inclination/transverse ranges of randomness were analyzed: 3°, 4°, 10°, 20° and 30°. The end-diastolic volumes (EDVs), ejection fractions (EFs), stroke volumes (SVs) and end-systolic fiber strains were compared to the normal case. The models were loaded to an end-systolic pressure of 120 mmHg. Complete details of the models may be found in [66,67].

The results of this model study are summarized in Table 53.3. These results suggest that the effects of disarray upon systolic function are pronounced whereas the diastolic function remains largely unchanged. Fiber disarray up to values of 4° exhibited no compromise in the hemodynamic systolic parameters. Disarray values of 10° or greater show ever-increasing degradation of systolic function, lower SVs and lower EFs. The fiber strain results serve as evidence that the loading on the fibers remains unchanged with ever-increasing disarray up to 4°. The models above 10° did not contract sufficiently to produce the necessary fiber strains. In contrast, the first principal strain results show that the wall strain values increase with decreasing systolic function. The mechanics of the LV demonstrated altered mechanical behavior that is due to the disarray even with nearly constant loading. In summary, fiber disarray alone, without the other factors associated with mechanical

P1: SFK/UKS P2: SFK Color: 4C
BLBK431-c53 BLBK431-Shenasa July 25, 2012 10:23 Trim: 276mm X 219mm Printer Name: Yet to Come

Table 53.3 Effect of myofiber disarray on cardiac function.

	Disarray range					
	0° (normal)	3°	4°	10°	20°	30°
EDV (ml)	117.5	117.5	117.6	117.6	117.6	117.6
SV (ml)	67	67	67	57	13	0
EF	57	57	57	49	10	0
Fiber strain	0.11	0.11	0.11	0.40	0.10	0.01
First principal strain	0.33	0.30	0.33	0.60	0.72	0.62

EDV, end-diastolic volume; EF, ejection fraction; SV, stroke volume.

dysfunction in hypertensive LVH, has a large negative effect upon systolic function, while diastolic function remains largely unchanged.

The global effect of disarray on the mechanics of the LV can be seen in reduced wall thickening, longitudinal shortening and twist. Figure 53.10 shows these effects for the normal case, and the cases of myofiber disarray equal to 4° and 20°. These results agree with changes in LV function reported in the literature [69] for non-hypertensive hypertrophic cardiomyopathy (HCM) which may also be indicative of changes for hypertensive LVH.

As an additional task, the 10° model was iteratively run with increasing contractility in order to determine how much more contraction force was necessary to achieve a normal end-systolic volume. The results of this study showed that a 26% increase in contraction stress was necessary in order for the 10° model to produce a normal end-systolic LV volume. This suggests that even this moderate amount of fiber disarray has a profound effect on cardiac performance.

Discussion and future directions

In this chapter, we have looked at LVH due to systemic hypertension from the aspect of myocardial fiber disarray. By employing *ex vivo* DT-MRI, we visualized in great detail and quantified the regional loss of myocardial fiber organization that was present in hypertrophied rat hearts, as opposed to controls. The results of this chapter correlate with results obtained three decades ago by using painstaking histology [24]. These histological results had also demonstrated the derangement of the normal pattern of the myocardial fibers in the lateral wall of adult SHRs. The outcomes of this study improve our understanding of the structural remodeling mechanisms that are associated with hypertensive LVH. Also, they open up possibilities in diagnosing this cardiac disorder. Future work will investigate the structural alterations that are associated with hypertensive LVH in younger rats.

Following our DT-MRI analysis, regional myofiber disarray was also observed in the posterior and anterior junction

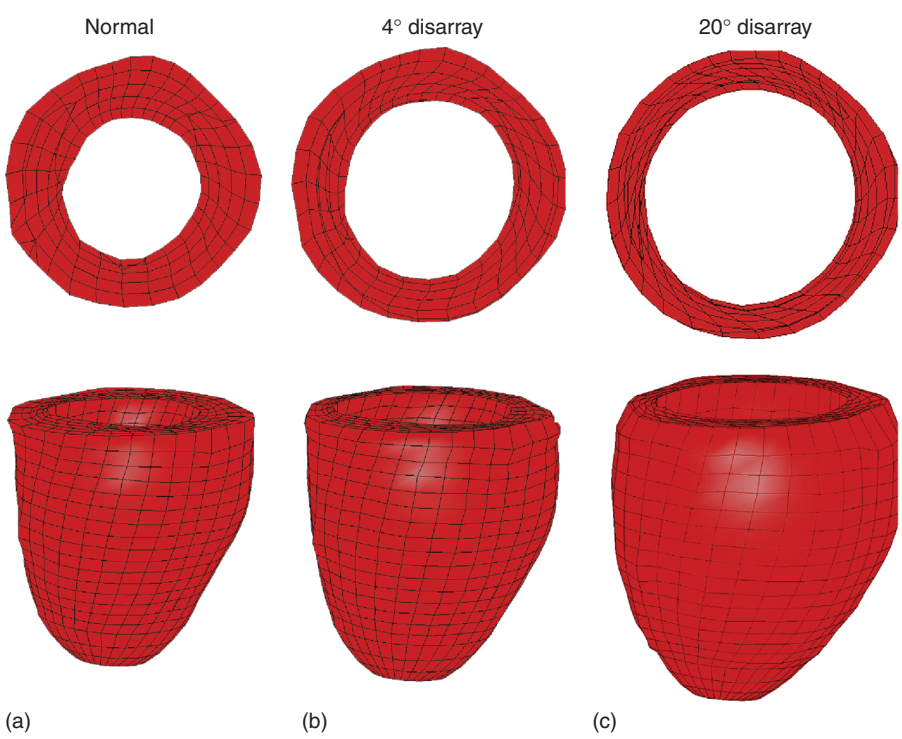

Figure 53.10 The models demonstrate the effects of fiber disarray on the wall mechanics of the left ventricle. There is a reduction in apical twist, wall thickening and wall shortening in the 4° (b) and the 20° (c) models compared with the normal model (a).

areas of the LV free wall and right ventricle (RV) free wall for both rats. This observation also correlates with previous histology findings [70]. In addition, it is a common practice in cardiology to avoid taking these junction areas into account when performing studies to establish a morphologic diagnosis of heart diseases [71]. Hence, with this in mind, we excluded this area from our analysis to avoid interpretation pitfalls.

In this study, DT-MRI was employed to elucidate changes in the microstructural organization that are associated with hypertensive LVH. However, other diffusion MRI protocols exist that further enhance the potential of DT-MRI for cardiac applications. Notably, Q-ball imaging [72] is one of them. Within a $100\,\mu m^3$ voxel, there can be approximately 100 fibers that potentially have differing orientations. Unlike DT-MRI, Q-ball imaging can resolve this intravoxel tissue orientation heterogeneity [73,74]. The laminar sheet characterization could also benefit from this technique [75]. Another high angular resolution technique, which is hypothesis-free and may infer intravoxel diffusion heterogeneity, is diffusion spectrum imaging (DSI) [76]. Finally, there are some other quite promising diffusion MRI methods that combine hindered and restricted modeling of water diffusion by using double-pulsed field gradient [77] or both low and high b-values [78] and might also allow a more detailed delineation of cardiac tissue. For an excellent review of diffusion modeling and protocols, see [79].

DT-MRI cardiac fiber tractography is a technique inherited from the study of fluids. Using this imaging technique, cardiac clinicians can determine the muscular tissue connectivity and its remodeling during the progression of certain diseases. DT-MRI cardiac fiber tractography was used to depict the alterations in the integrity of cardiac muscle microstructure due to hypertensive LVH. Myocardial fiber tracking results were provided by employing the streamline tracking method. Other more advanced techniques have been introduced with a view to overcoming some inherent noise limitations of the streamlining methods. One such example is the probabilistic tractography methods that treat the fiber orientation as a random variable, the distribution of which is predicted by either simulations or Bayesian inference or Monte Carlo markov chain methods. Furthermore, global approaches that use global criteria and are markedly less sensitive to noise have been applied. For a thorough review of the cardiac tractography methods, see [80] and references therein. All enhanced imaging protocols described in the previous paragraph lend themselves well for conducting enhanced heart tractography. Currently DSI has been shown to generate some interesting visualizations [81–83].

DT-MRI cardiac fiber tractography has great potential to improve the non-invasive diagnosis and treatment of cardiac disease. However, for the moment there is a lot of uncertainty associated with this technique (due to noise, motion artifacts, imaging artifacts and partial volume effects). In addition, many different DT-MRI imaging protocols are available. While useful qualitative conclusions can be drawn from DT-MRI cardiac fiber tractography, it would perhaps be prudent to defer exclusive reliance on this imaging technique for fine operations (such as surgical planning) until a gold standard regarding imaging protocols is established and all related uncertainties are clarified.

In this chapter we have also addressed cardiac function issues. In particular, by using FE modeling, we showed that the irregular arrangement of myofibers in the hypertensive LVH has a profound effect on the mechanical properties of the heart. Notwithstanding these attractive results, additional studies need to be conducted to definitely establish the exact relationship between the myocardial fiber disarray in hypertensive LVH and the alterations in cardiac mechanical behavior during systole or diastole.

By focusing only on factors that are related to the structural remodeling, this chapter has neglected a number of other interesting issues that also contribute to the degradation of the mechanical function in the hypertensive LVH. Myocardial energy metabolism is notably one of them. In particular, changes in myocardial energy metabolism (e.g., in high-energy phosphate metabolism or fatty acid β-oxidation) have been shown [84,85] to have an impact on the functional abnormalities in the hypertensive LVH. The energy metabolism effects are beyond the scope of this chapter, but how to incorporate these effects accurately into the problem formulation could be a research area in itself.

In this chapter, ex vivo *DT-MRI and FE mechanical modeling were employed independently of each other. However, the advent of DT-MRI has revived the interest in the muscular compartment and the role it may play in altering the ventricular function. In other words, the joint use of DT-MRI imaging and modeling has great potential.* For example, we may build a more realistic model of the heart *by directly using* ex vivo *DT-MRI data (usually combined with some interpolation method) to incorporate the preferential arrangement of the cardiac cells [*86–88*]. This is* easily achievable because both the anatomical inputs (i.e., geometry and myocardium fiber architecture) are obtained from the same heart. As a result, the DT-MRI analysis framework does not rely to a great extent on image processing. Subsequently, this DT-MRI-based anatomic model might be combined with *in vivo* tagged MRI deformation data and conductance current pressure recordings into a computational model that studies ventricular mechanics [89–95]. However, due to differences in myocardial geometry between *in vivo* and *ex vivo* imaging, some registration method (e.g., host mesh fitting [89]) should be used to ensure the accurate embedding of the DT-MRI-derived myofiber architecture. In general, DT-MRI, by providing a more detailed and realistic description of the microscopic cardiac tissue morphology, may boost our confidence in a more reliable model-based prediction of its mechanical function. Moreover, it may shed light on the

P1: SFK/UKS P2: SFK Color: 4C
BLBK431-c53 BLBK431-Shenasa July 25, 2012 10:23 Trim: 276mm X 219mm Printer Name: Yet to Come

underlying structural basis of heart progressive dysfunction under the hypertensive LVH. In any case, in the long run a benefit of the joint use of modeling and imaging is better understanding, diagnosis and treatment.

Conclusion

A large percentage of hypertensive subjects will present with LVH as a result of the prolonged exposure to increased ventricular load. The presence of LVH in this patient population heralds many feared cardiovascular complications. A prevalent morphological characteristic of LVH caused by arterial hypertension is myocardial fiber disarray. The well-ordered and smoothly varying spatial alignment of myocardial fibers that characterizes the normal myocardium no longer exists in the areas of myofiber disarray.

In recent years, DT-MRI has emerged as a powerful tool to delineate the alterations in complex cardiac tissue connectivity that certain diseases brings forth. FE computational models of the heart have also evolved as ideal hosting environments to observe the mechanical function of the heart.

We used *ex vivo* DT-MRI to delineate the regional disorientation of myocardial fibers that is present in the excised heart of a SHR, as opposed to a control. Our aim was to provide fiber tracking results enabling a precise and detailed visualization of the microstructural alterations after hypertensive LVH. We also attempted to quantify the degree of spatial malalignment of cardiomyocytes by using a scatter matrix-based approach. Then, we examined the mechanical aspects of the myocardial fiber disarray. Although the etiology of the mechanical dysfunction in hypertensive LVH is multi-factorial, we performed a model-based study to investigate whether myofiber disarray alone has an impact on the decline of the mechanical function associated with hypertensive LVH.

We conclude that DT-MRI allows a unique insight into the microstructural alterations after hypertensive LVH. It improves our understanding of the structural remodeling mechanisms that are associated with this cardiac disorder. Also, it opens up possibilities in the diagnosis of hypertensive LVH. In addition, our FE simulation results show that the irregular configuration of myocardial fibers has a profound effect on the cardiac mechanics.

Chapter video clips

Video clip 53.1 The helix-like fiber structure of a healthy adult rodent heart as inferred by DT-MRI.

Video clip 53.2 The laminar structure of a healthy adult rodent heart as inferred by DT-MRI.

Video clip 53.3 The hypertensive LVH-induced extensive disarray is detectable by DT-MRI.

Acknowledgements

We thank Kathleen M. Brennan, DVM, in the Department of Radiotracer Development and Imaging Technology at Lawrence Berkeley National Laboratory for preparation of the excised heart samples, and Edward W. Hsu, PhD, in the Department of Bioengineering at the University of Utah for acquiring the rat DT-MRI data used in this chapter. This work was supported in part by the National Institutes of Health, NIH grant number R01EB007219 and the Director, Office of Science, Office of Biological and Environmental Research, Biological Systems Science Division of the U.S. Department of Energy under Contract No. DE-AC02-05CH11231.

References

1 Rohmer D, Sitek A, Gullberg GT. Reconstruction and visualization of fiber and laminar structure in the normal human heart from ex vivo diffusion tensor magnetic resonance imaging (DT-MRI) data. *Invest Radiol* 2007;**42**:777–89.
2 Basser PJ, Mattiello J, LeBihan D. MR diffusion tensor spectroscopy and imaging. *Biophys J* 1994;**66**:259–67.
3 Jones DK. *Diffusion MRI: Theory, Methods, and Applications.* New York: Oxford University Press, 2011.
4 Nicholson C, Rice ME. The migration of substances in the neuronal microenvironment. *Ann New York Acad Sci* 1986;**481**: 55–68.
5 Axelrod D, Koppel DE, Schlessinger J, *et al.* Mobility measurement by analysis of fluorescence photobleaching recovery kinetics. *Biophys J* 1976;**16**:1055–69.
6 Hsu EW, Healy LJ, Einstein DR, Kuprat AP. Imaging-based assessment and modeling of the structures of the myocardium. In: Guccione JM, Kassab GS, Ratcliffe MB (eds) *Computational Cardiovascular Mechanics – Modeling and Applications in Heart Failure*. New York: Springer, 2009: pp. 23–39.
7 Pierpaoli C, Jezzard P, Basser PJ, Barnett A, Di Chiro G. Diffusion tensor MR imaging of the human brain. *Radiology* 1996;**201**:637–48.
8 Filidoro L, Dietrich O, Weber J, *et al.* High-resolution diffusion tensor imaging of human patellar cartilage: Feasibility and preliminary findings. *Magn Reson Med* 2005;**53**:993–8.
9 Ries M, Jones RA, Dousset V, Moonen CTW. Diffusion tensor MRI of spinal cord. *Magn Reson Med* 2000;**44**:884–92.
10 Wedeen VJ, Reese TG, Napadow VJ, Gilbert RJ. Demonstration of primary and secondary muscle fiber architecture of the bovine tongue by diffusion tensor magnetic resonance imaging. *Biophys J* 2001;**80**:1024–8.
11 Eyal E, Furman-Haran E, Degani H. 3-D tracking of the mammary ductal tree using diffusion tensor MR imaging. In *Proceedings of the 16th Scientific Meeting of the International Society for Magnetic Resonance in Medicine (ISMRM 2008)*; May 3–9, 2008; Toronto, Ontario, Canada: p. 588.

12 Sinha S, Sinha U. In vivo diffusion tensor imaging of the human prostate. *Magn Reson Med* 2004;**52**:530–7.
13 Zijta FM, Froeling M, van der Paardt MP, *et al.* Feasibility of diffusion tensor imaging (DTI) with fibre tractography of the normal female pelvic floor. *Eur Radiol* 2011;**21**:1243–9.
14 Budzik JF, LeThuc V, Demondion X, *et al.* In vivo MR tractography of thigh muscles using diffusion imaging: initial results. *Eur Radiol* 2007;**17**:3079–85.
15 Schwenzer NF, Steidle G, Martirosian P, *et al.* Diffusion tensor imaging of the human calf muscle: distinct changes in fractional anisotropy and mean diffusion due to passive muscle shortening and stretching. *NMR Biomed* 2009;**22**:1047–53.
16 Frindel C, Robini M, Schaerer J, Croisille P, Zhu YM. A graph-based approach for automatic cardiac tractography. *Magn Reson Med* 2010;**64**:1215–29.
17 Basser PJ, Pajevic S, Pierpaoli C, Duda J, Aldroubi A. In vivo fiber tractography using DT-MRI data. *Magn Reson Med* 2000;**44**:625–32.
18 Zhukov L, Barr AH. Oriented tensor reconstruction: Tracing neural pathways from diffusion tensor MRI. *Proceedings of the IEEE Visualization (Vis 2002)*; Oct 27–Nov 12002; Boston, MA, USA: pp. 387–94.
19 Grossman W, Jones D, McLaurin LP. Wall stress and patterns of hypertrophy in the human left ventricle. *J Clin Invest* 1975;**56**:56–64.
20 Lorell BH, Carabello BA. Left ventricular hypertrophy: Pathogenesis, detection, and prognosis. *Circulation* 2000;**102**:470–9.
21 Gradman AH, Alfayoumi F. From left ventricular hypertrophy to congestive heart failure: Management of hypertensive heart disease. *Prog Cardiovasc Dis* 2006;**48**:326–41.
22 Drazner MH. The progression of hypertensive heart disease. *Circulation* 2011;**123**; 327–34.
23 Tingleff J, Munch M, Jakobsen TJ, *et al.* Prevalence of left ventricular hypertrophy in a hypertensive population. *Eur Heart J* 1996;**17**:143–9.
24 Kawamura K, Kashii C, Imamura K. Ultrastructural changes in hypertrophied myocardium of spontaneously hypertensive rats. *Jpn Circ J* 1976;**40**:1119–45.
25 Mirsky I, Pfeffer JM, Pfeffer MA, Braunwald E. The contractile state as the major determinant in the evolution of left ventricular dysfunction in the spontaneously hypertensive rat. *Circ Res* 1983;**53**:767–78.
26 Weber KT, Janicki JS, Schroff SG, *et al.* Collagen remodeling of the pressure-overloaded, hypertrophied nonhuman primate myocardium. *Circ Res* 1988;**62**:757–65.
27 Schwartzkopff B, Motz W, Frenzel H, *et al.* Structural and functional alterations of the intramyocardial coronary arterioles in patients with arterial hypertension. *Circulation* 1993;**88**:993–1003.
28 Engelmann GL, Vitullo JC, Gerrity RG. Morphometric analysis of cardiac hypertrophy during development, maturation, and senescence in spontaneously hypertensive rats. *Circ Res* 1987;**60**:487–94.
29 Kehat I, Molkentin JD. Molecular pathways underlying cardiac remodeling during pathophysiological stimulation. *Circulation* 2010;**122**:2727–35.
30 Díez J, Frohlich ED. A translational approach to hypertensive heart disease. *Hypertension* 2010;**55**:1–8.
31 Patterson C, Portbury AL, Schisler JC, Willis MS. Tear me down – role of calpain in the development of cardiac ventricular hypertrophy. *Circ Res* 2011;**109**:453–62.
32 Greenwood JP, Scott EM, Stoker JB, Mary DASG. Hypertensive left ventricular hypertrophy: relation to peripheral sympathetic drive. *J Am Coll Cardiol* 2001;**38**:1711–17.
33 Schlaich MP, Kaye DM, Lambert E, *et al.* Relation between cardiac sympathetic activity and hypertensive left ventricular hypertrophy. *Circulation* 2003;**108**:560–5.
34 Atlas SA. The renin-angiotensin aldosterone system: pathophysiological role and pharmacologic inhibition. *J Manag Care Pharm* 2007;**13**:S9–20.
35 Gosse P. Left ventricular hypertrophy as a predictor of cardiovascular risk. *J Hypetens* 2005;**23**:S27–33.
36 Bacharova L. Electrical and structural remodeling in left ventricular hypertrophy–A substrate for a decrease in QRS voltage? *Ann Noninvasive Electrocardiol* 2007;**12**:260–73.
37 Levy D, Garrison RJ, Savage DD, *et al.* Prognostic implications of echocardiographically determined left ventricular mass in the Framingham Heart Study. *N Engl J Med* 1990;**322**:1561–6.
38 McLenachan JM, Henderson E, Morris KI, Dargie HJ. Ventricular arrhythmias in patients with hypertensive left ventricular hypertrophy. *N Engl J Med* 1987;**317**:787–92.
39 Edvardsen T, Rosen BD, Pan L, *et al.* Regional diastolic dysfunction in individuals with left ventricular hypertrophy measured by tagged magnetic resonance imaging – The Multi-Ethnic Study of Atherosclerosis (MESA). *Am Heart J* 2006;**151**:109–14.
40 Takeuchi M, Borden WB, Nakai H, *et al.* Reduced and delayed untwisting of the left ventricle in patients with hypertension and left ventricular hypertrophy: a study using two-dimensional speckle tracking imaging. *Eur Heart J* 2007;**28**:2756–62.
41 Brilla CG, Janicki JS, Weber KT. Impaired diastolic function and coronary reserve in genetic hypertension role of interstitial fibrosis and medial thickening of intramyocardial coronary arteries. *Circ Res* 1991;**69**:107–15.
42 Nishimura H, Kubo S, Nishioka A, *et al.* Left ventricular diastolic function of spontaneously hypertensive rats and its relationship to structural components of the left ventricle. *Clin Sci (Lond)* 1985;**69**:571–9.
43 Fouad FM, Slominski JM, Tarazi RC. Left ventricular diastolic function in hypertension: relation to left ventricular mass and systolic function. *J Am Coll Cardiol* 1984;**3**:1500–6.
44 Piella G, De Craene M, Bijnens BH, *et al.* Characterizing myocardial deformation in patients with left ventricular hypertrophy of different etiologies using the strain distribution obtained by magnetic resonance imaging. *Rev Esp Cardiol* 2010;**63**: 1281–91.
45 Nishimura K, Okayama H, Inoue K, *et al.* Direct measurement of radial strain in the inner-half layer of the left ventricular wall in hypertensive patients. *J Cardiol* 2012;**59**:64–71.
46 Tan H, Zheng G, Li L, *et al.* Impaired left ventricular synchronicity in hypertensive patients with ventricular hypertrophy. *J Hypertens* 2008;**26**:553–9.
47 Kannel WB. Role of blood pressure in cardiovascular morbidity and mortality. *Prog Cardiovasc Dis* 1974;**17**:5–24.
48 Mehta SK, Rame JE, Khera A, *et al.* Left ventricular hypertrophy, subclinical atherosclerosis, and inflammation. *Hypertension* 2007;**49**:1385–91.

49 Salcedo EE, Marwick TH, Korzick DH, *et al.* Left ventricular hypertrophy sensitizes the myocardium to the development of ischaemia. *Eur Heart J* 1990;**11**:G72–8.

50 Otterstad JE. Ischaemia and left ventricular hypertrophy. *Eur Heart J* 1993;**14**:G2–6.

51 Chambers J. Left ventricular hypertrophy. *BMJ* 1995;**311**: 273–4.

52 Gould KL, Carabello BA. Why angina in aortic stenosis with normal coronary arteriograms? *Circulation* 2003;**107**:3121–3.

53 Guccione JM, Kassab GS, Ratcliffe MB. *Computational Cardiovascular Mechanics – Modeling and Applications in Heart Failure.* New York: Springer, 2009.

54 Imamura K. Ultrastructural aspect of left ventricular hypertrophy in spontaneously hypertensive rats: a qualitative and quantitative study. *Jpn Circ J* 1978;**42**:979–1002.

55 Takemura G, Fujiwara H, Mukoyama M, *et al.* Expression and distribution of atrial natriuretic peptide in human hypertrophic ventricle of hypertensive hearts and hearts with hypertrophic cardiomyopathy. *Circulation* 1991;**83**:181–90.

56 Chahine R, Hanna J, Bassil C, *et al.* Beneficial effect of taurine in spontaneous hypertensive rats: Implication of its antioxidant activity. *Afr J Pharm Pharmacol* 2010;**4**:874–7.

57 Nepomnyashchikh LM, Lushnikova EL, Semenov DE. Peculiarities of intracellular regeneration of cardiomyocytes during plastic myocardial insufficiency. *Bull Exp Biol Med* 2000; **130**:1011–16.

58 Tanaka M, Fujiwara H, Onodera T, *et al.* Pathogenetic role of myocardial fiber disarray in the progression of cardiac fibrosis in normal hearts, hypertensive hearts and hearts with hypertrophic cardiomyopathy. *Jpn Circ J* 1987;**51**:624–30.

59 Okamoto K, Aoki K. Development of a strain of spontaneously hypertensive rats. *Jpn Circ J* 1963;**27**:282–93.

60 Papadakis NG, Xing D, Huang CLH, *et al.* A comparative study of acquisition schemes for diffusion tensor imaging using MRI. *J Magn Reson* 1999;**137**:67–82.

61 Koay CG, Chang LC, Carew JD, *et al.* A unifying theoretical and algorithmic framework for least squares methods of estimation in diffusion tensor imaging. *J Magn Reson* 2006;**182**:115–25.

62 Hsu EW, Muzikant AL, Matulevicius SA, *et al.* Magnetic resonance myocardial fiber-orientation mapping with direct histological correlation. *Am J Physiol Heart Circ Physiol* 1998;**274**:H1627–34.

63 Streeter DD. Gross morphology and fiber geometry of the heart. In: Berne RM, Sperelakis N (eds) *Handbook of Physiology, The Cardiovascular System, The Heart.* Bethesda, MD: American Physiological Society, 1979: pp. 61–112.

64 Wang J, Lin Y, Wai Y, *et al.* Visualization of the coherence of the principal diffusion orientation: an eigenvector-based approach. *Magn Reson Med* 2008;**59**:764–70.

65 Wu YC, Field AS, Chung MK, *et al.* Quantitative analysis of diffusion tensor orientation: Theoretical framework. *Magn Reson Med* 2004;**52**:1146–55.

66 Veress AI, Segars WP, Tsui BMW, Gullberg GT. Incorporation of a left ventricle finite element model defining infarction into the XCAT imaging phantom. *IEEE Trans Med Imaging* 2011;**30**:915–27.

67 Veress AI, Segars WP, Weiss JA, *et al.* Normal and pathological NCAT image and phantom data based on physiologically realistic left ventricle finite-element models. *IEEE Trans Med Imaging* 2006;**25**:1604–16.

68 Tseng WYI, Dou J, Reese TG, Wedeen VJ. Imaging myocardial fiber disarray and intramural strain hypokinesis in hypertrophic cardiomyopathy with MRI. *J Magn Reson Imaging* 2006;**23**:1–8.

69 Maier SE, Fischer SE, McKinnon GC, Hess OM, Krayenbuehl HP, Boesiger P. Evaluation of left ventricular segmental wall motion in hypertrophic cardiomyopathy with myocardial tagging. *Circulation* 1992;**86**:1919–28.

70 Kuribayashi T. Spontaneously occuring hypertrophic cardiomyopathy in the rat. I. Pathologic features. *Jpn Circ J* 1987;**51**: 573–88.

71 van der Bel-Kahn J. Muscle fiber disarray in common heart diseases. *Am J Cardiol* 1977;**40**:355–64.

72 Tuch DS. Q-ball imaging. *Magn Reson Med* 2004;**52**:1358–72.

73 Dierckx H, Benson AP, Gilbert SH, *et al.* Intravoxel fibre structure of the left ventricular free wall and posterior left-right ventricular insertion site in canine myocardium using Q-ball imaging. In: Ayache N, Delingette H, Sermesant M (eds) *Proceedings of the 5th International Conference on Functional Imaging and Modeling of the Heart; Jun 3–5 2009; Nice, France. Berlin: Springer-Verlag*, 2009: pp. 495–504.

74 Shi Y, Jiang Y, Hsu EW. Comparison of diffusion tensor and Q-ball imaging of the canine myocardium. In: *Proceedings of the 15th Scientific Meeting of the International Society for Magnetic Resonance in Medicine (ISMRM 2007)*; May 19–25 2007; Berlin, Germany: p. 1470.

75 Dierckx H, Benson AP, Gilbert SH, *et al.* Dual Q-ball imaging reveals intravoxel orientation distribution functions for laminar structures in the heart. In: *Proceedings of the 17th Scientific Meeting of the International Society for Magnetic Resonance in Medicine (ISMRM 2009)*; April 18–24 2009; Honolulu, HI, USA: p. 3546.

76 Wedeen VJ, Hagmann P, Tseng WYI, *et al.* Mapping complex tissue architecture with diffusion spectrum magnetic resonance imaging. *Magn Reson Med* 2005;**54**:1377–86.

77 Shemesh N, Ozarslan E, Komlosh ME, Basser PJ, Cohen Y. From single-pulsed field gradient to double-pulsed field gradient MR: gleaning new microstructural information and developing new forms of contrast in MRI. *NMR Biomed* 2010;**23**:757–80.

78 Assaf Y, Freidlin RZ, Rohde GK, Basser PJ. New modeling and experimental framework to characterize hindered and restricted water diffusion in brain white matter. *Magn Reson Med* 2004;**52**:965–78.

79 Jensen JH, Helpern JA. Special issue: progress in diffusion-weighted imaging: concepts, techniques, and applications to the central nervous system. *NMR Biomed* 2010;**23**:659–904.

80 Frindel C, Robini M, Schaerer J, *et al.* A graph-based approach for automatic cardiac tractography. *Magn Reson Med* 2010;**64**:1215–29.

81 Sosnovik DE, Wang R, Dai G, *et al.* Diffusion MR tractography of the heart. *J Cardiovasc Magn Reson* 2009;**11**:47–61.

82 Sosnovik DE, Wang R, Dai G, *et al.* Diffusion spectrum MRI tractography reveals the presence of a complex network of residual myofibers in infarcted myocardium. *Circ Cardiovasc Imaging* 2009;**2**:206–12.

83 Wang TT, Kwon HS, Dai G, Wang R, *et al.* Resolving myoarchitectural disarray in the mouse ventricular wall with

diffusion spectrum magnetic resonance imaging. *Ann Biomed Eng* 2010;**38**:2841–50.

84 Lamb HJ, Beyerbacht HP, van der Laarse A, *et al.* Diastolic dysfunction in hypertensive heart disease is associated with altered myocardial metabolism. *Circulation* 1999;**99**:2261–7.

85 Lopaschuk GD, Ussher JR, Folmes CDL, *et al.* Myocardial fatty acid metabolism in health and disease. *Physiol Rev* 2010;**90**:207–58.

86 Gurev V, Lee T, Constantino J, *et al.* Models of cardiac electromechanics based on individual hearts imaging data. Image-based electromechanical models of the heart. *Biomech Model Mechanobiol* 2011;**10**:295–306.

87 Seemann G, Keller DUJ, Weiss DL, Dossel O. Modeling human ventricular geometry and fiber orientation based on diffusion tensor MRI. In: Murray A (ed.) *Proceedings of the 33rd Annual International Conference of Computers in Cardiology*, Sep 17–20, 2006; Valencia, Spain: pp. 801–4.

88 Xia L, Dou JH, Gong YL, Deng DD. Simulation analysis of mechanical properties of the canine heart with bundle branch block based on a 3-D electromechanical model. In: Murray A (ed.) *Proceedings of the 34th Annual International Conference of Computers in Cardiology*; Sep 30–Oct 3, 2007, Durham, NC, USA: pp. 673–6.

89 Wang VY, Lam HI, Ennis DB, *et al.* Modelling passive diastolic mechanics with quantitative MRI of cardiac structure and function. *MedIA* 2009;**13**:773–84.

90 Wang VY, Lam HI, Ennis DB, *et al.* Cardiac active contraction parameters estimated from magnetic resonance imaging. In: Camara O, Pop M, Rhode K, et al. (eds) *Proceedings of the 1st International Workshop on Statistical Atlases and Computational Models of the Heart (STACOM 2010) and Cardiac Electrophysiological Simulation Challenge (CESC 2010)*; Sept 20, 2010; Beijing, China. Berlin: Springer-Verlag, 2010: pp.194–203.

91 Augenstein KF, Cowan BR, LeGrice IJ, *et al.* Method and apparatus for soft tissue material parameter estimation using tissue tagged magnetic resonance imaging. *J Biomech Eng* 2005;**127**:148–57.

92 Sermesant M, Delingette H, Ayache N. An electromechanical model of the heart for image analysis and simulation. *IEEE Trans Med Imaging* 2006;**25**:612–25.

93 Sermesant M, Moireau P, Camara O, *et al.* Cardiac function estimation from MRI using a heart model and data assimilation: advances and difficulties. *MedIA* 2006;**10**:642–56.

94 Walker JC, Ratcliffe MB, Zhang P, *et al.* MRI-based finite-element analysis of left ventricular aneurysm. *Am J Physiol Heart Circ Physiol* 2005;**289**:H692–700.

95 Walker JC, Ratcliffe MB, Zhang P, *et al.* Magnetic resonance imaging-based finite element stress analysis after linear repair of left ventricular aneurysm. *J Thorac Cardiovasc Surg* 2008;**135**:1094–102.